

Holographic optical coherence imaging of rat osteogenic sarcoma tumor spheroids

Ping Yu, Mirela Mustata, Leilei Peng, John J. Turek, Michael R. Melloch, Paul M. W. French, and David D. Nolte

Holographic optical coherence imaging is a full-frame variant of coherence-domain imaging. An optoelectronic semiconductor holographic film functions as a coherence filter placed before a conventional digital video camera that passes coherent (structure-bearing) light to the camera during holographic readout while preferentially rejecting scattered light. The data are acquired as a succession of *en face* images at increasing depth inside the sample in a fly-through acquisition. The samples of living tissue were rat osteogenic sarcoma multicellular tumor spheroids that were grown from a single osteoblast cell line in a bioreactor. Tumor spheroids are nearly spherical and have radial symmetry, presenting a simple geometry for analysis. The tumors investigated ranged in diameter from several hundred micrometers to over 1 mm. Holographic features from the tumors were observed in reflection to depths of 500–600 μm with a total tissue path length of approximately 14 mean free paths. The volumetric data from the tumor spheroids reveal heterogeneous structure, presumably caused by necrosis and microcalcifications characteristic of some human avascular tumors. © 2004 Optical Society of America
OCIS codes: 170.4500, 110.4500, 090.2880, 190.5330, 190.5970.

1. Coherence-Domain Imaging and *En Face* Data Formats

Coherence-domain imaging is performed with several acquisition formats that use short-coherence interferometry to image inside scattering media.^{1–7} The most common format is based on optical coherence-domain reflectometry⁸ with a rapid-scan delay line that uses heterodyne detection to demodulate the coherent interference and differentiate it from the scattered background. This generates the so-called A scan that produces an optical echo gram as a function of depth. When the A scan is combined with lateral scanning along a single dimension, it generates the B scan that converts reflectometry data into a section

as a function of depth and one lateral space dimension. The B scan is the most common data format for coherence-domain image visualization. A stack of B scans produces a data volume with voxels that can be rendered in three dimensions for enhanced visualization approaches. Any subset can be extracted from the data volume, including the *en face* format that gives a two-dimensional image at a fixed depth and is also known as the C scan.

En face images also can be generated directly by use of a fixed delay and by means of rapidly scanning in two lateral directions. The fixed delay requires a different demodulation approach, such as heterodyne detection with a frequency-shifted reference. When combined with on-chip smart-pixel technology with parallel data acquisition, this can generate video-rate movies.⁹ The smart-pixel arrays currently operate at 58×58 pixels.¹⁰

A direct *en face* imaging approach with much higher pixel density uses direct acquisition into a CCD camera.¹¹ By acquisition of several successive images at a fixed delay but with different reference phases, the coherent part of the image can be differentiated from the diffuse scattered background. This generates images with pixel numbers over a million. The phase modulation and acquisition can also be fast enough to approach video rates. The technical drawbacks of this approach are the need for

P. Yu is with the Department of Physics, University of Missouri, Columbia, Missouri 65211. M. Mustata, L. Peng, M. R. Melloch, and D. D. Nolte (nolte@physics.purdue.edu) are with the Department of Physics and School of Electrical and Computer Engineering, Purdue University, West Lafayette, Indiana 47907-2036. J. J. Turek is with the Department of Basic Medical Sciences, School of Veterinary Medicine, Purdue University, West Lafayette, Indiana 47907-1246. P. M. W. French is with the Photonics Group, Department of Physics, Imperial College of Science, Technology and Medicine, London SW7 2BW, UK.

Received 15 December 2003; accepted 12 March 2004.

0003-6935/04/254862-12\$15.00/0

© 2004 Optical Society of America

interferometric stability during the time to acquire a single image set and the limited dynamic range in current CCD cameras that limits the detection sensitivity.

Spatial interference in holograms presents an alternative *en face* method to demodulate the coherent interference between the signal and the reference beams. Holography has long been recognized as a technique for imaging through inhomogeneous media, for example, with phase-conjugate holography.^{12,13} Techniques for making transmission holograms through fog were proposed that relied on the incoherence of scattered light.^{14,15} Holography with laser pulses that gate the first-arriving light through scattering media was proposed early¹⁶ and was later refined for biomedical applications.^{17,18}

This early research relied for the most part on static holograms that needed to be exposed and developed and then illuminated with a reconstruction laser, all of which removed any possibility of probing into scattering media in real time. This set the stage for the development of holographic optical coherence imaging (OCI) that relies on dynamic holographic media that are constantly updating. Photorefractive materials are particularly attractive as dynamic holographic coherence gates because they are not saturated by the incoherent background the way that holographic film or CCDs are. The photorefractive effect also supports dynamic holography with refresh rates easily compatible with video frame rates and is capable of much higher rates.^{19,20}

Holographic OCI was initially developed with bulk photorefractive crystals and volume holograms.²¹ However, the implementation with volume holograms made readout difficult because of the need to match the Bragg diffraction angle. In addition, the updating rates for the crystals were relatively slow. These initial problems were removed when the photorefractive crystals were replaced with photorefractive semiconductor devices.²²

Photorefractive quantum wells (PRQWs) are semiconductor optoelectronic devices^{23–25} that use semiconductor growth processes to produce semiconductor structures that have enhanced optical properties based on quantum localization of electrons in very thin layers (7.5 nm). The enhanced optical properties make these devices candidates for many adaptive interferometric and imaging applications.^{22,26–29}

Holographic OCI in PRQW devices was first demonstrated with video-rate image acquisition,^{30,31} with later-increases in acquisition speed up to 470 frames/s²⁰ for an acquisition time of only 2 ms, which would make it possible to image fast changes in metabolic processes. The imaging depth range for OCI is currently approximately 15 mean free paths in double pass.³¹ The axial (longitudinal) resolution of OCI has achieved 14 μm with short-coherence sources,³² and the lateral resolution is typically 10 μm ,³³ although this is a function of the optics and the magnification. Resolution down to 1 μm in a high-magnification configuration should be possible.

The first holograms of light reflected from within living tissue were demonstrated by holographic OCI applied to multicellular tumor spheroids.³⁴ The data were recorded in so-called fly-throughs, in which a succession of *en face* images were acquired at successive depths from within the spheroids. When the fly-throughs were halted at a specified depth, called a punctuated fly-through, quantitative information related to cellular and subcellular motility could be extracted from the statistics of the speckle holograms.³⁵ This has important consequences for potential intraoperative applications of holographic OCI for the assaying of biologically significant areas of tissue at low magnification and for extraction of subcellular motility information from within the tissue.

In this paper we present a complete technical description of holographic OCI applied to image living tissue. The samples are rat osteogenic sarcoma tumor spheroids that are grown from a single osteoblast cell line in a bioreactor. The spheroids are nearly spherical and have radial symmetry, presenting a simple geometry for analysis. They are characterized by an outer shell of healthy cells in close contact with nutrients and oxygen in the growth medium, a thin inner shell of apoptotic cells undergoing programmed cell death, and an inner core of necrotic tissue with microcalcifications and necrotic voids filled with extracellular debris. The tumors range in diameter from several hundred micrometers to over a millimeter.

The technical details of OCI as they relate to this tumor imaging application are described in Section 2, including image acquisition and filtering to remove artifacts from dust and imperfections on the current generation of holographic film, plus procedures for next-generation film fabrication that will remove most of these defects. The details of the tumor growth and structure are presented in Section 3. In section 4 we present the holographic fly-through data sets of several tumors, including three-dimensional visualization of the tumors and statistical analysis of the observed holographic features.

2. Holographic Optical Coherence Imaging Experimental Setup

Holographic OCI shares much in common with optical coherence tomography (OCT). Both are coherence-domain imaging techniques that use short-coherence light sources to define depth and longitudinal resolution. Both seek to differentiate coherent backscatter from diffuse backscatter by use of coherent interference with a reference wave followed by demodulation. In OCT, the preferred mode is temporal heterodyne detection at a single point with signal filtering to perform demodulation. In OCI, the interferometric detection mode is spatial heterodyne across a full field of view with holographic readout (diffraction) performing the role of demodulation.

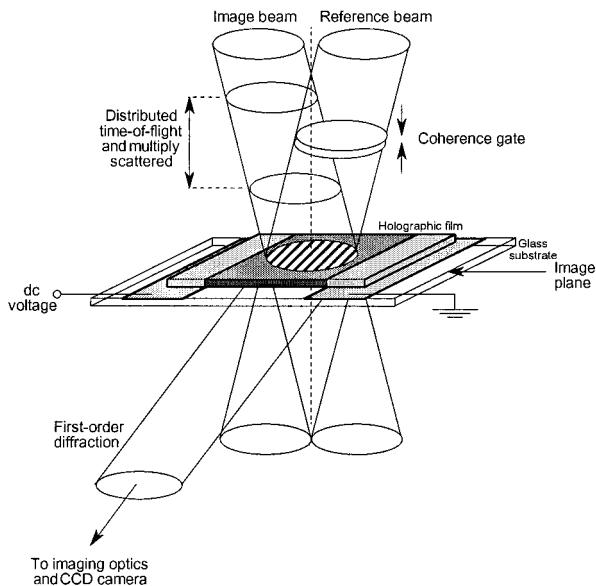


Fig. 1. Principle of holographic coherence gating in a PRQW film. The film responds only to the gradient in intensity rather than to the intensity itself. This allows the weak holographic fringes to be recorded while the high-intensity diffuse light passes through. In the degenerate four-wave mixing geometry, the reference is also the readout, diffracting from the film into the camera. This approach is direct imaging with the hologram acting as a coherence filter that depth gates coherent backscattered light from the diffuse specimen.

A. Holography as Spatial Heterodyne

The coherence gating function of holographic OCI is shown schematically in Fig. 1. The image field, containing spatially and temporally coherent light as well as diffuse light, is incident on the dynamic holographic film at one angle, and a plane reference field is incident from a different angle. The finite crossing angle between the image field and the reference field produces interference fringes at the film with a fringe spacing of

$$\Lambda = \frac{\lambda}{2 \sin \theta}, \quad (1)$$

where θ is the half-angle between the beams and λ is the wavelength. Only the coherent part of the image field produces the interference whereas the diffusely scattered light presents a random speckle that is typically outside the coherence length and hence produces no persistent fringes. The periodic fringes modulate the optical properties of the photorefractive film through the gradient of the intensity,²⁴ making the film partially insensitive to high background. (The incoherent background still presents an erasure mechanism, but does not saturate the dynamic range of the film as it would for films that respond to intensity rather than gradient in intensity.)

The periodic modulation in the optical properties of the film in turn behaves as a diffraction grating that diffracts the reference field in the direction of a CCD camera, where it is imaged onto the CCD plane. In

principle, only the coherent image-bearing part of the image field produces the hologram and is read out by the reference field. Because none of the diffusely scattered light from the image field reaches the camera, this is a so-called background-free mixing geometry. In practice, the image field contains speckle that does have spatial intensity gradients that can write holograms and diffract light. However, the spatial bandwidth of this background disperses the diffracted light and limits the amount of background captured by the reconstruction optics. Furthermore, this background speckle can be time averaged at the camera by use of a vibrating mirror with a frequency slower than the holographic film, but faster than the frame rate of the camera.

The preceding description of holographic recording and readout can also be phrased from the point of view of spatial heterodyne and demodulation. The image field presents a spectrum of spatial frequencies, and the interference fringes present a spatial carrier frequency that is modulated by the image spectrum. This is shown schematically in Fig. 2(a), for the case of image speckle alone and in the presence of the reference wave. The Fourier transform of Fig. 2(a) is shown in Fig. 2(b) compared with an incoherent background speckle that is chosen to be 100 times stronger in intensity. The image field modulation of the spatial carrier frequency produces sidebands that can rise by many orders of magnitude above the background spectrum at that spatial frequency. In the example in Fig. 2, there is an 8 order-of-magnitude discrimination between coherent image speckle and incoherent background at the carrier frequency. It is in this sense that holographic recording is background free. The process of demodulation is simply diffraction of the reference from the image-modulated carrier into the imaging optics of the camera. There is a constraint that the spatial frequency of the carrier must be higher than the spatial bandwidth of the image. In practice, this requires that each coherent speckle from the signal wave contain at least three interference fringes. In practice, dust and other defects on the holographic film provide other more serious sources of background, but these can be removed by postacquisition filtering.

With this analogy, holographic OCI uses spatial heterodyne in much the same way that OCT uses temporal heterodyne. However, there is a fundamental difference between temporal and spatial mixing. In spatial heterodyne, many optical modes are interfering in parallel whereas in temporal heterodyne only a single optical mode is active at a time. The increase in parallelism from OCT to OCI can be as large as A/λ^2 , where A is the field of view of OCI and λ is the wavelength. For $A = 1 \text{ mm}^2$, the gain in parallelism is 10^6 , which is roughly the pixel count on a CCD camera. In this sense, the spatial multiplexing of OCI provides an increase in voxel rate by at least 6 orders of magnitude, all other factors being the same (which is not true in practice).

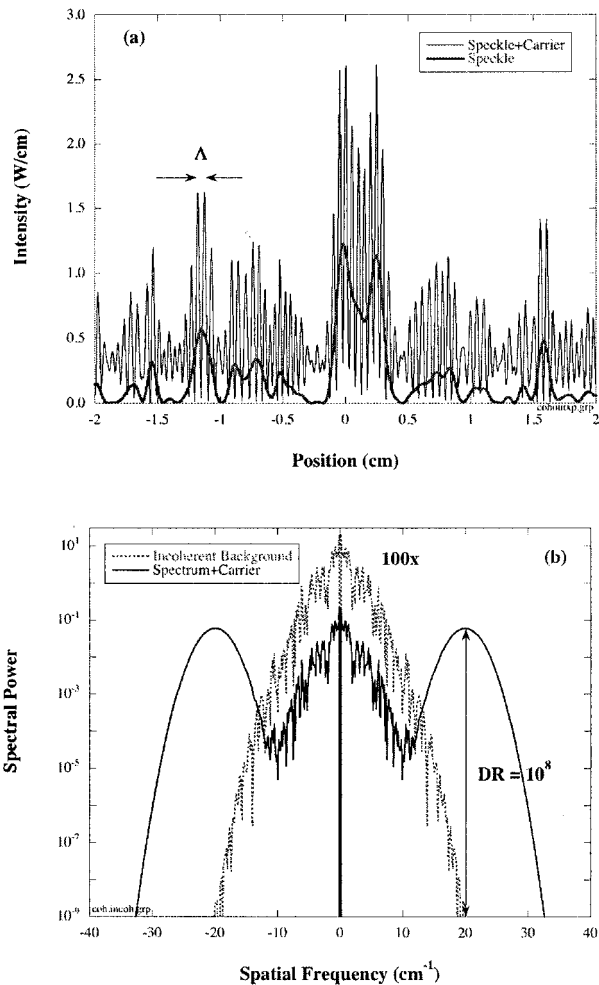


Fig. 2. Simulation of holography as spatial heterodyne. (a) The image speckle from the diffuse object is spatially modulated through interference with the reference by a carrier wave with a spatial carrier frequency $1/\Lambda$. (b) The spatial spectrum of the image (dotted curve) and hologram (solid curve) shows the strong sidebands in the hologram that rejects the zero order by many orders of magnitude. DR, dynamic range.

B. Degenerate Four-Wave Mixing Optical Layout

The experimental setup for the degenerate mixing is shown in Fig. 3. It uses a low-coherence light source in a modified Mach-Zehnder interferometer with an imaging-system in the sample arm and a delay stage in the reference arm, with a PRQW-device and a CCD camera. The low-coherence light source used in our OCI experiments is a diode-pumped Ti:sapphire laser (Clark MXRNJA-5) operating at a wavelength of 837 nm with a 120 fs pulse duration and a repetition rate of 100 MHz. The center wavelength and the bandwidth of the laser span the excitonic spectral bandwidth of the PRQW. Samples are positioned in the signal arm in a reflection geometry.

A mirror in the reference arm of the interferometer is vibrated at approximately 500 Hz by a piezoelectric stack. The purpose of this moving mirror is to eliminate pixel cross talk and stray speckle (nonimage speckle) in the *en face* images. This vibration has a

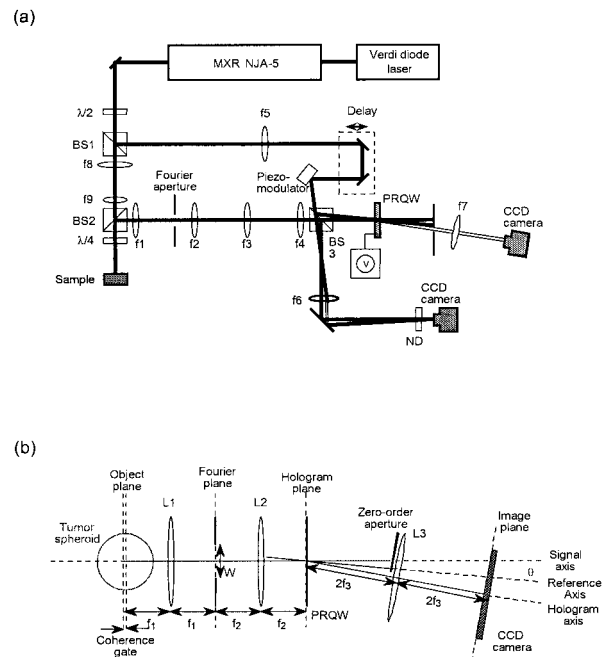


Fig. 3. Holographic OCI experimental layout. (a) The general layout shows the illumination source and the modified Mach-Zehnder interferometer in a degenerate four-wave mixing configuration. The sample is interrogated in reflection and the polarization is selected by the polarizing beam splitter (BS). A key element in the reference arm is the piezomirror that vibrates at a rate that is tracked by the holographic film, but not by the camera, thereby time averaging the parasitic cross talk (non-image-bearing) speckle. (b) Shows the details of the Fourier optics used to filter the optical images. The hologram is recorded in an image plane. ND, neutral density filter.

sufficiently low frequency that allows the holographic film to track the induced fringe motion without diminishing the diffracted intensity, while the frequency is sufficiently high that the camera time averages over many cycles, averaging out the interpixel speckle. This feature of holographic OCI (different response times between the holographic film and the camera) allows it to reject interpixel cross talk while retaining the full spatial coherences (and resulting speckle) arising from structure in the tissue. This presents one advantage of the holographic OCI relative to phase-shifted full-field optical coherence microscopy,³⁶ which does not differentiate between the two types of speckle.

The nonlinear mixing in the PRQW device is in a degenerate four-wave mixing configuration. In degenerate mixing, the readout beam is the reference beam (hence it has a frequency degenerate with the signal and reference waves), whereas in nondegenerate mixing (used by the Imperial College group) the readout beam is a separate beam that may have a different wavelength and come from a different light source. Both configurations image the first-order diffracted beam of the readout into a CCD camera.

The nondegenerate configuration has some advantages over the degenerate. First, use of a separate readout wavelength allows conventional filters to re-

ject the background as well as incoherently scattered light of the reference off of imperfections in the holographic film. Second, it is possible to use any photon energy for the signal and reference that is above the bandgap of the semiconductor device (approximately 1.5 eV) to write the holographic gratings, allowing spectroscopic information to be extracted from the sample. The readout remains tuned to the resonant wavelength of the photorefractive device.

The degenerate configuration has different advantages. First, only a single light source is needed for both hologram writing and readout, simplifying the optical setup. Second, use of the reference as the readout prevents additional hologram erasure (that is experienced in the nondegenerate case because of the independent readout). In the degenerate configuration, higher reference intensities generate brighter holographic reconstructions, whereas in the nondegenerate configuration the reference must be matched to the signal intensity to prevent hologram erasure. In practice, this leads to a factor of 6-dB (in the CCD camera) higher hologram readout for the degenerate configuration and eliminates any need to adjust the reference power if the signal power is changing due to changes in the optical density of the specimen across the field of view. In our application, tumor spheroids present just such a variation in optical thickness because of their spherical shape. Our use of the degenerate configuration therefore helps us to record balanced images across a tumor section.

Because OCI is a full-frame parallel acquisition mode, the input laser needs to be distributed over large areas on the sample. This requires a higher-power laser in OCI to keep intensities comparable to conventional OCT at each pixel. The Ti:sapphire femtosecond laser provides sufficient power to acquire holograms of a highly scattering specimen. In addition, a telescope is used in the signal arm of the interferometer to decrease the diameter of the input laser beam by a factor of 3. The laser beam diameter on the sample is approximately 1.0 mm with a power of 200 mW. Two lenses are used to form a 4- F image system to project the image of the sample onto the holographic film. A spatial filter is located at the Fourier plane of the image system to reject part of the scattered light from the sample. The signal interferes with the reference at the PRQW when the optical path lengths between the signal and the reference are matched to within a coherence length of the laser by an adjustment of the translation stage in the reference. The interference fringes are imprinted onto the holographic film.

The active layer of the PRQW device is grown by molecular beam epitaxy, which consists of a multiple quantum-well layer composed of a 100 period 70-Å GaAs well and a 60-Å $\text{Al}_{0.2}\text{Ga}_{0.8}\text{As}$ barrier on a semi-insulating GaAs substrate. After the growth, the layer is epoxied on glass and the substrate is removed by etching. An electric field (dc of 10 kV/cm) is applied in the plane of the device. This configuration is called the transverse-field geometry that uses the

Franz-Keldysh effect. The holograms are reconstructed by degenerate four-wave mixing in the PRQW. The first-order diffracted signal from the reference is imaged onto the surface of a cooled CCD camera (RTE/CCD 1317, Princeton Instruments) with a 150-mm focal-length lens, and an aperture is used to cut off the zero orders. The acquisition time in these experiments is set to 100 ms for a field of view that covers 157×185 pixels with a fivefold signal averaging to give a total time per acquired frame of 500 ms. The efficiency of the four-wave mixing is optimized by adjustment of the wavelength and bandwidth of the laser, the size and positions of the apertures, and the relative intensities between the signal and the reference.

The reference delay stage is controlled by a stepper motor that is scanned in fixed steps to allow the acquisition of image frames from successive depths in the samples. The depth resolution of the OCI system is 34 μm , determined by measurement of the cross-correlation widths of the diffracted signals by use of a single reflective surface at the sample position. The transverse resolution is 19 μm , determined by measurement of the hologram of a U.S. Air Force test chart. The basic data set from a single fly-through is a data cube of approximately 200 by 200 *en face* pixels by 200 depth sections with 10- μm spacing.

The details of the Fourier optics in the imaging arm of the interferometer are shown in Fig. 3(b). The image from the tumors is relayed to the PRQW device through four lenses with a demagnification of 3:1. A Fourier plane is available for spatial filtering through an aperture. This aperture controls the spatial coherence and speckle size at the quantum-well plane. For efficient hologram readout, there must be more than approximately three fringes per speckle.

C. Postacquisition Image Processing

Although holographic OCI is in principle background free, imperfections in the holographic film that arise during the numerous device fabrication stages scatter light from the hologram plane into the camera, producing a static background. This scatter tends to be highly localized (dust particles on the film or small air bubbles in the epoxy supporting the semiconductor film) and hence produces hot spots in the CCD image. The holograms between these hot spots are not affected and may be read out essentially background free. If a hot spot does occur within the field of view of a tumor spheroid, it can be filtered with postacquisition processing, unless the hot spot saturates the camera and causes data dropout. This dropout is minimized in practice when relatively clean portions of the film are selected to image through. This pragmatic approach is not ideal, but leads to successful acquisition of images from inside the tumor spheroids. In the future, commercially manufactured PRQWs will become available that would mostly eliminate this current limitation.

The static scatter from imperfections in the holographic film is suppressed in each frame by back-

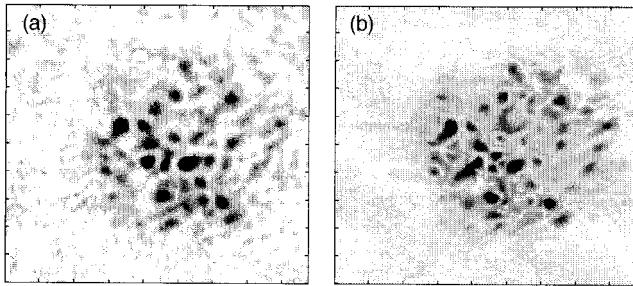


Fig. 4. Postacquisition image processing. (a) The background-subtracted holographic X,Y section of tumor T0508A-03 with a diameter of 600 μm that is 200 μm deep inside the tumor. (b) The same section after Fourier filtering along the z axis to remove the remaining background.

ground subtraction, followed by a high-pass Fourier filter along the z axis of the acquired data cube. The scatter is independent of the delay and therefore is present as a dc baseline shift in the hot pixels. The data are conditioned prior to background subtraction and Fourier filtering by means of logarithmically saturating the high background while the linear scaling of the holographic image is retained. The image is transformed according to

$$A^T = y_0 \ln(1 + A/y_0), \quad (2)$$

where y_0 is a scale factor, roughly three times the magnitude of the highest tissue hologram brightness. This transformation achieves logarithmic saturation of large pixel values, and the linear holograms are retained through the approximation $\ln(1 + x) \approx x$ to yield linear scaling for small x from the holograms of interest. The logarithmically conditioned holographic section near the top of a tumor is shown in Fig. 4(a) after background subtraction. Post-Fourier-filtered images can be presented either as thresholded images on the in-phase (real) part of the filtered data or as the modulus of the filtered data, as shown in Fig. 4(b). These filtered images constitute the final data for the tumor spheroid.

3. Rat Osteogenic Sarcoma Tumor Spheroids

For instrument development and modification for the study of biological tissue, it is necessary to have a steady and abundant source of living tissue. It is feasible to use animals (i.e., rodents), but that would require killing numbers of animals, involve anesthesia during the imaging process, and complicate tissue collection. Fortunately, there is a well-characterized *in vitro* model that can be used to simulate multicellular tissues.^{37–42} Multicellular spheroids of normal cells or neoplastic cells (tumor spheroids) are balls of cells that can be easily cultured up to several millimeters in size *in vitro*. The spheroids can be used to simulate the optical properties of a variety of tissues such as the epidermis and various epithelial tissues and can be used to simulate the histological and metabolic features of small nodular tumors in the early avascular stages of growth.⁴² As tumor spheroids are cultured, they undergo cell apo-

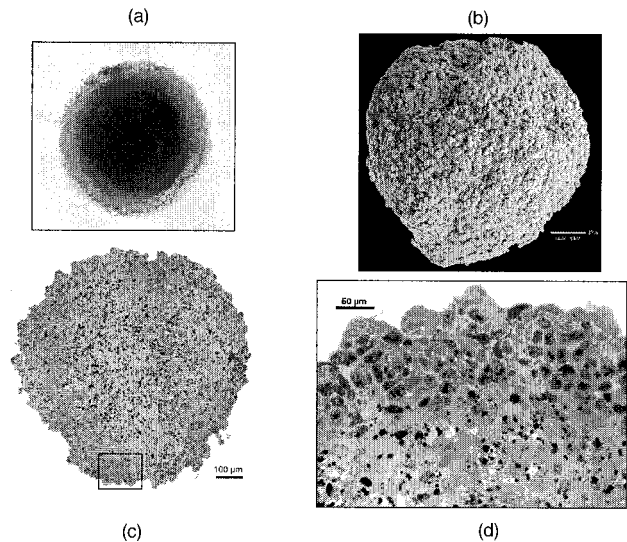


Fig. 5. (a) Transmission low-magnification microscope image of a 700- μm -diameter tumor spheroid. (b) Conventional scanning electron micrograph of a different 700- μm tumor spheroid showing individual cells on the surface. (c) Optical thin-section micrographs of a 900- μm -diameter tumor spheroid, showing a thin outermost shell of healthy cells approximately 100 μm thick, with innercore necroses and microcalcifications. (d) Enlargement of the rectangular section showing details of the healthy shell and the inner necroses.

ptosis and necrosis in their center in a manner similar to naturally occurring nodular tumors.³⁸ In addition, if certain tumor cell lines are used, the spheroids will develop microcalcifications that can bear similarities to those found in the human breast.

To create tumor spheroids, rat osteogenic sarcoma UMR-106 cells were cultured in Dulbecco's modified Eagle's medium with 10% fetal calf serum, 100-u/ml penicillin, 100- $\mu\text{g}/\text{ml}$ streptomycin, and 1% L -glutamine in sterile 60-mm non-tissue-culture plastic dishes. The non-tissue-culture plastic causes the tumor cells to form the spheroids in 7–10 days, which are then transferred to a rotating bioreactor (Synthecon, Houston, Texas) where they are maintained in suspension for several weeks. The spheroids can be grown up to several millimeters in diameter and are thus large enough to simulate the thickness of different mammalian tissue (skin epidermis is 70–120 μm thick over most of the human body). An advantage of this continuous culture model is that fresh spheroids of varying size are easily prepared on a daily basis. Overall, the tumor spheroids provide a reasonable tissue model that does not require special handling of animal subjects.

Tumor spheroids are shown in Fig. 5 by various forms of conventional microscopy. A transmission low-magnification microscope image of a 700- μm -diameter tumor is shown in Fig. 5(a). The tumor is highly spherical and translucent. Diffuse light can be seen around the edges in the transmission image, but little light passes through the full diameter. A low-resolution scanning electron microscope image of

a different 700- μm -diameter tumor spheroid is shown in Fig. 5(b). The tumor is roughly spherical with approximately 10- μm -size cells on the surface. To image the interior structure by conventional microscopy, spheroids were fixed with 3% phosphate-buffered glutaraldehyde, postfixed with 1% phosphate-buffered osmium tetroxide and embedded in epoxy resin (Polybed 812, Polysciences, Warrington, Pennsylvania). Spheroids were serially sectioned (1 μm) and stained with Toluidine blue for light microscopic examination. A medial optical section of a 900- μm -diameter tumor spheroid is shown in Fig. 5(c), where individual cells at the perimeter are clearly visible. A shell of healthy cells approximately 100 μm thick on the outside (in close proximity to nutrients and oxygen) encloses the necrotic core. A blow-up of an outer region is shown in Fig. 5(d) showing the healthy shell in more detail and a portion of the necrotic region. Deeper inside the tumor are regions of cellular apoptosis and necrosis that become larger and more frequent toward the center of the spheroids.

Overall, the tumor spheroids exhibit a roughly radial symmetry, but are mostly homogeneous without strong structural features or distinct morphology changes that can be detected with histology. This has the disadvantage that correlative histology cannot be performed to connect features observed in the OCI data sets with features observed in the histology. The OCI data sets will exhibit generally featureless speckle images arising from the homogeneously distributed necroses inside the spheroid. On the other hand, the radial symmetry has the advantage that statistical trends, such as density of necroses as a function of radius, shared by the OCI data sets and the histology should correlate positively, as we show in Sub section 4.C.

4. Holographic Optical Coherence Imaging of Tumor Spheroids

We have acquired data on numerous tumor spheroids ranging in diameter from 300 μm to over 1 mm. The principal data-acquisition mode is called a fast fly-through. This mode consists of a stack of frames, each from successively deeper inside the tumor. The interframe time is short (1500 ms in the current system) relative to the hologram temporal correlation times (several seconds) and thus is a succession of freeze frames of both persistent (structural) and variable (cell motility) features. This mode is used to provide fingerprint volumetric data sets of tumors. Consecutive fly-throughs of the same tumor followed by image cross correlation provide repeatability tests and preliminary measures of persistence versus variability. For presentation of the data, we extract selected X,Y (*en face*) and Y,Z (B-scan) sections from the data volume, as well as three-dimensional volumetric visualizations. A quantitative analysis of the tumor speckle structure is presented that shows a clear trend in the speckle brightness as a function of radius from the geometric center of the tumors with increas-

ing brightness correlating with regions of greater necrosis observed histologically.

A. Tumor Sections and Volumetric Rendering

During imaging, the tumors are immersed in growth medium and rest on the bottom of a plastic Petri dish. The Petri dish is not optically flat and presents a speckled reflection that is used to find the zero path in the reference arm and used to accurately locate the bottom of the tumor spheroids. The data from a single tumor spheroid consist of a data volume composed of a stack of *en face* images. The coordinate system defining the voxel location uses X,Y for the *en face* image and Z for increasing depth starting from the beginning of the reference scan. The top of the tumor is imaged first, followed by the bulk of the tumor, and finally passing through the Petri dish support at the bottom of the tumor.

The typical voxel count of a fly-through data set is $200 \times 200 \times 200 = 8^6$ voxels, corresponding to a typical volume of $1 \text{ mm} \times 1 \text{ mm} \times 2.5 \text{ mm} = 2.5 \text{ mm}^3$, acquired in a total of 100 s of integration time. This gives a voxel rate of 80,000 voxels/s and a volume rate of $25 \times 10^6 \mu\text{m}^3/\text{s}$. The voxel count is currently limited by the nonoptimized CCD handshaking with the acquisition computer. In principle, no computer acquisition is needed because this is a direct imaging approach and could be recorded directly to a conventional digital tape. The achievable rate with our current system when recorded directly is 1×10^6 pixels per frame \times 200 frames per fly-through = 200×10^6 voxels in a 100-s total integration time. This would yield a voxel rate of 2×10^6 voxels/s. For comparison, a smart pixel OCT array has achieved 5×10^6 voxels/s.⁹ However, an OCI rate five to ten times higher should be practical with additional improvements in holographic film quality and camera sensitivity.

Selected X,Y sections from a 600- μm -diameter tumor T0508A-03 are shown in Fig. 6, showing every fifth frame beginning at the top of the tumor on the upper left and proceeding past the middle of the tumor to the Petri reflection on the lower right. The top of the tumor is at frame 68 and the Petri dish is at frame 150. The tumor was chemically cross linked with glutaraldehyde, preventing cellular motion during the fly-through. The size of the individual frames is 175 pixels along X and 200 pixels along Y . The lateral scale is set by 5.2 $\mu\text{m}/\text{pixel}$ at the sample. The shadow of the tumor can clearly be seen in the diffuse Petri dish reflection. The Fourier aperture in the optical system cuts off the specular reflection from the Petri dish that would otherwise saturate the film. The middle of the tumor is at frame 108 (approximately 300 μm deep or 600 μm of total path). The holograms are still strong at this depth, but weaken for deeper planes, disappearing around frame 140 (approximately 550 μm deep or 1.1 mm of total path).

A selection of Y,Z (B-scan) sections is shown in Fig. 7 for the same 600- μm tumor beginning at the side of the tumor and scanning through the tumor, showing

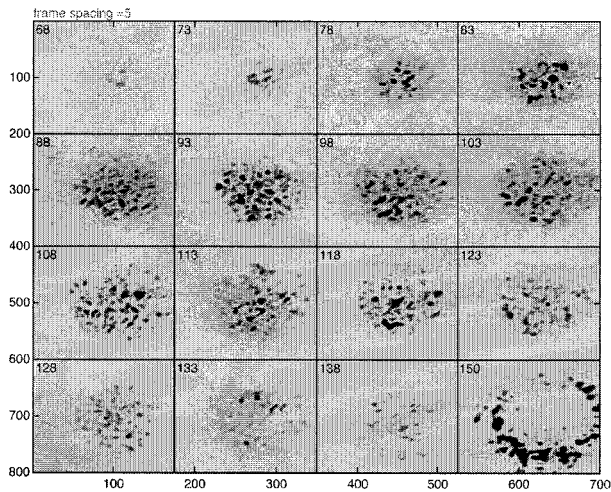


Fig. 6. Selected X,Y (*en face*) sections of a 600- μm -diameter tumor (T0508A-03). The fly-through has 200 frames with a depth step of 7.4 μm (in the tumor). Only every fifth section is shown. The top of the tumor is at frame 68, and the Petri dish reflection is at frame 150. The medial cross section is at frame 108.

every eighth frame starting at the top left and proceeding to the bottom right. The aspect ratio is not 1:1, giving the spheroid an oval appearance. The Petri dish reflection is on the right of each frame. The medial cross section is near frame 100. An enlargement of the medial frame at $X = 106$ is shown in Fig. 8(a) and is compared with an integrated projection in Fig. 8(b). The integrated projection is the sum of all B scans and provides a pseudotransillumination image of the full tumor. A medial X,Y cross section at a depth of 300 μm from the top is shown in Fig. 8(c). It is clear from Fig. 8 that the strongest scattering occurs from the center of the tumor, which is statistically consistent with the results of histology. Medial cross sections from representative tumor

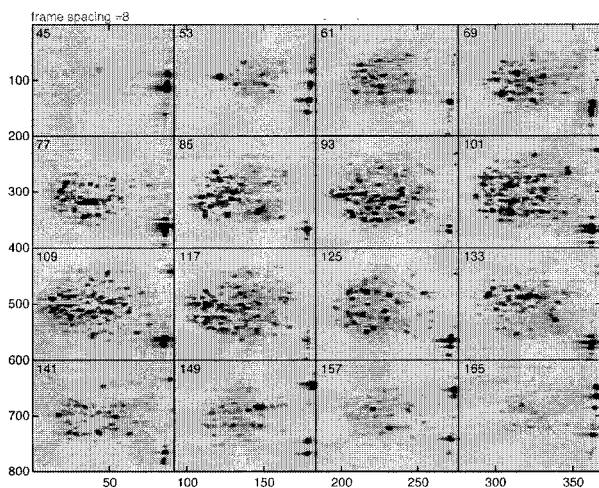


Fig. 7. Reconstructed Y,Z sections (B scans) through the same spheroid and data volume of Fig. 6. The aspect-ratio is not 1:1, showing the tumor as elliptical. The Petri dish reflection is on the right of each frame, and the illumination is from the left. The medial cross section is frame 100.

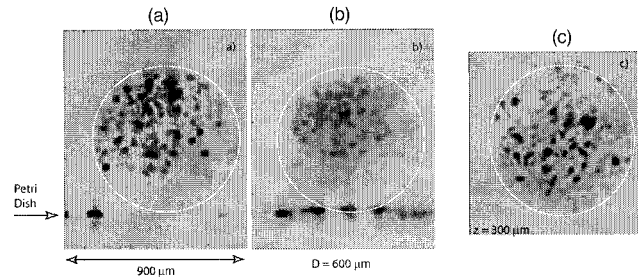


Fig. 8. Selected views of the 600- μm -diameter tumor spheroid of Figs. 6 and 7. (a) Medial cross section presented as a Y,Z B scan. Note the size and shape of the shadow on the back of the tumor and on the Petri dish reflection. (b) Integrated view produced by summation of the data volume along the x axis. This is equivalent to transillumination data. (c) Medial *en face* cross section at a depth of 300 μm from the top of the tumor.

spheroids are shown in Fig. 9. Each image is auto-scaled separately.

On the basis of these images, we estimate that we are able to penetrate nearly 550 μm deep into the tumor along the center line, with a total tissue path of 1.1 mm. The momentum transport length in the tumor spheroids has been measured independently to be 80 μm . We are therefore able to penetrate an optical thickness of approximately 14 mean free paths in this application. This is consistent with the best calibrated performance demonstrated previously for holographic OCI.³¹

The holographic OCI B scan of the 600- μm -diameter tumor spheroid is compared with an OCT B scan of a different tumor in Fig. 10. The OCT system was a rapid-scan system at Case Western Reserve University in Cleveland, Ohio, that was

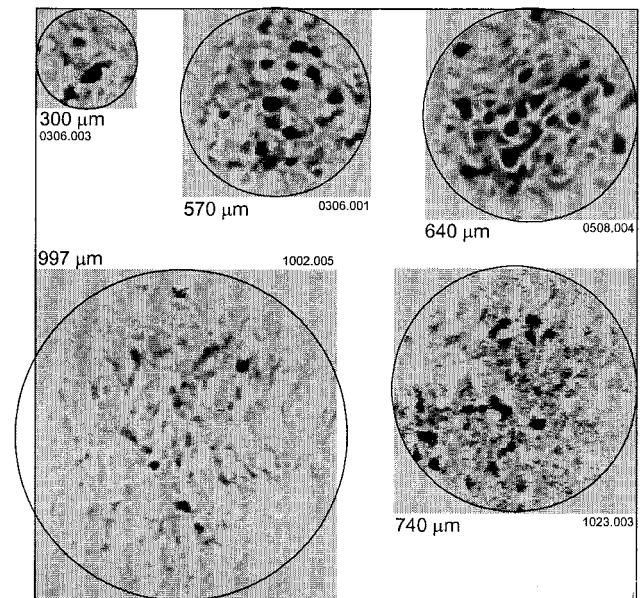


Fig. 9. Medial X,Y sections of five different tumors of increasing size. Each image is auto-scaled separately (the small tumor presents the weakest hologram, whereas the strongest holograms come from the 1-mm-diameter tumor).

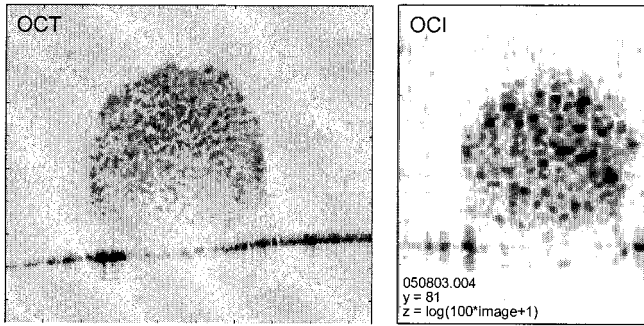


Fig. 10. Comparison between OCT and holographic OCI data sets. These are medial cross sections of different tumors. The OCT system was a rapid-scan system operating at a 1.3- μm -wavelength (courtesy of A. Rollins, Case Western University). The superior spatial resolution and signal-to-noise ratio of the OCT B scan is evident, but the OCI image is a single section of a data volume. The spatial resolution difference is not fundamental, and improvements in OCI should approach the spatial resolution of OCT. Improvements in holographic film quality will improve sensitivity and the signal-to-noise ratio.

optimized for voxel rate and resolution, but not sensitivity. The OCT data are presented on a pseudo-linear scale for direct comparison with OCI. Both data sets share the same overall appearance, except for the image resolution, which is related to the different resolutions of the systems. Both show the shadow at the deep portions of the tumor, and both show stronger scattering from the center of the tumor. The superior spatial resolution and signal-to-noise ratio of the OCT B scan is evident, but the OCI image is a single section of an entire data volume. The spatial resolution difference is not fundamental, and improvements in OCI should approach the spatial resolution of OCT. Improvements in holographic film quality will in addition improve sensitivity and the signal-to-noise ratio.

A volumetric reconstruction of a 640- μm -diameter tumor spheroid is shown in Fig. 11 (sample 0508.004). The shadow on the Petri dish is clearly visible beneath the tumor. The tumor consists of an outer shell of weak holographic speckle (seen as a dim

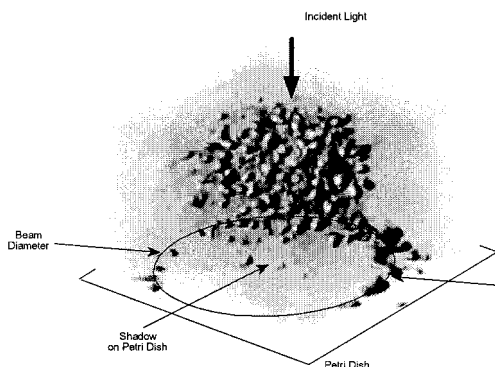


Fig. 11. Three-dimensional volumetric reconstruction of a 640- μm -diameter of a multicellular tumor spheroid showing the shadow on the Petri dish and the internal holographic features of the necrotic core.

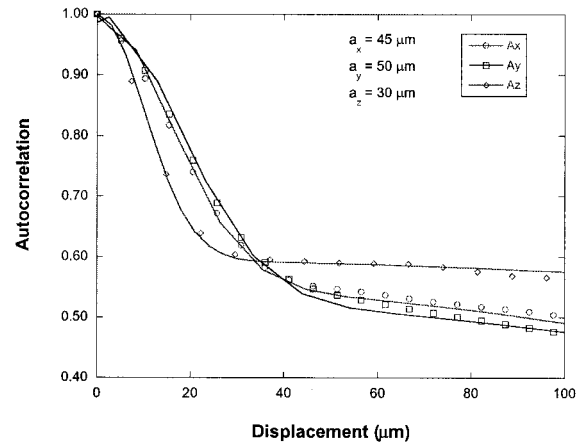


Fig. 12. Average autocorrelation analysis of the X,Y images of a fly-through with line plots of the autocorrelation peak, showing lateral resolution of approximately 50 μm and longitudinal resolution of 30 μm .

halo surrounding the outside of the tumor), with larger and stronger holographic speckle occurring toward the center of the spheroid. This follows the structure observed in the histology of similar tumors discussed in Section 3.

B. Image Correlation Analysis

Autocorrelation measures the average feature size both laterally and longitudinally. The average autocorrelations for tumor T0508A-03 are shown in Fig. 12. The lateral full width at half-maximum sizes are 45 and 50 μm for the X and Y directions, respectively. We obtained the longitudinal speckle size by performing the autocorrelation analysis in the Y,Z sections. The Z autocorrelation width is found to be 30 μm , which is consistent with the coherence length of the light source.

The lateral and longitudinal feature sizes of the holograms are consistent with the resolution of the optical system from which we can conclude that the dominant holographic features are primarily due to subresolution objects, i.e., a collection of scattering objects that have a size smaller than the optical resolution. Any long-range structure that would represent a specific structure internal to the tumor (such as extended necrotic voids with sizes larger than the resolution size of the imaging), if present, is much weaker and would appear as sidelobes in the autocorrelation traces. Therefore the tumor images observed in the holographic OCI data sets most likely arise from subresolution structural features (cell membranes, microcalcifications, nuclei, organelles). We currently see no strong evidence for the observation of a specific macroscopic structure inside the tumors. This conclusion must remain tentative until holographic OCI can be performed in microscopy with cellular resolution, which is the subject of future research. It is important to reiterate that the holograms are not composed of random speckle because of our use of the vibrating mirror in the reference arm

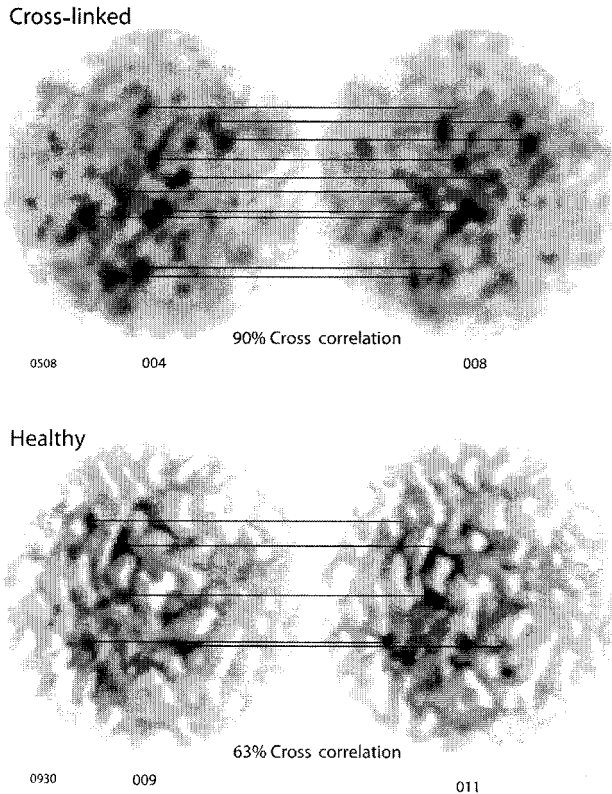


Fig. 13. Consecutive fly-through X,Y pseudotransillumination cross sections of a cross-linked tumor (top) and a healthy tumor (bottom). The holographic features in the cross-linked tumor are highly repeatable. In the healthy tumor, some features are persistent, but most are not. The dynamic nature of the healthy tumor arises from cellular motility and can be used as an index of cellular health.

that time averages random speckle at the CCD camera.

The cross correlation between two data sets on the same tumor gives a measure of similarity. Conversely, by taking the cross correlation between two different tumors, we can obtain a measure of dissimilarity. Clearly, the similarity should be significantly greater between two identical tumors compared with two different tumors. Two integrated X,Y projections for the same chemically fixed tumor taken approximately 30 min apart are compared in Fig. 13 (top). A similar structure is apparent in both projections. Two consecutive fly-throughs of a healthy tumor are shown in Fig. 13 (bottom). In this case, some similar structure is observed, but there are noticeable differences. Clearly, the state of health of the tumor (healthy compared with chemically cross-linked) is reflected in the repeatability observed in consecutive fly-throughs. This observation is quantified in the data cross correlation for the two sets, shown in Fig. 14. The cross correlation between the fly-throughs of the chemically fixed tumor shows a strong autocorrelation peak that approaches 90%, whereas the cross correlation of the fly-throughs of the healthy tumor show only a weak peak slightly above 60%. Finally,

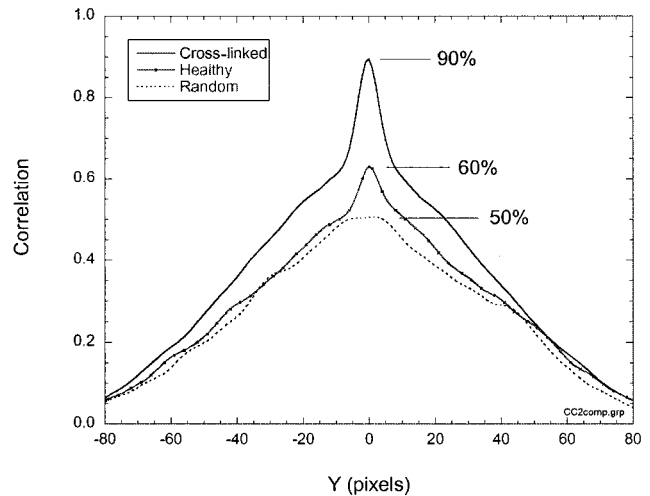


Fig. 14. Cross correlations of the consecutive fly-throughs of Fig. 13. The cross-linked tumor shows an autocorrelation peak of 90%, whereas the healthy tumor (with dynamic speckle) shows a correlation of only 60% relative to a random 50% cross correlation between two dissimilar tumors.

the cross correlation between two different tumors shows no peak at all above the 50% background. The broad background of the cross-correlation traces relates to the size of the tumor, which is the same in all three traces.

From this quantitative cross-correlation analysis, we can conclude that when the tumors are chemically fixed, they produce static specklelike holographic features with high stability and repeatability even over hours. The structure may arise from subresolution features in the tumor, but the structure is repeatable. This therefore represents an important test for the holographic technique when applied to tissue. However, for living tumors, the cellular and subcellular motility produces a constantly changing specklelike pattern arising from cellular motility (most likely motion of the cellular membranes). It is interesting to note that cellular and subcellular motion that manifest itself as dynamic (time-varying) speckle in this application becomes a cellular thermometer, providing cellular-scale information even though the spatial resolution is incapable of resolving individual cells. This may make it possible to holographically image over broad areas and still record information relevant to cellular processes.

C. Speckle Image Statistics: Comparison with Histology
As stated above, the image arises from subresolution structure in the sample. In the TEM images discussed in Section 2, the observed microcalcifications were typically smaller than the OCI imaging resolution ($40\ \mu\text{m}$) and therefore are not likely to be resolvable. To explore these aspects of the tumor holograms, we studied the statistics of the holographic feature brightness and compared them with the statistics obtained by histology on similar (although not identical) tumors.

To perform a statistical analysis on the speckle

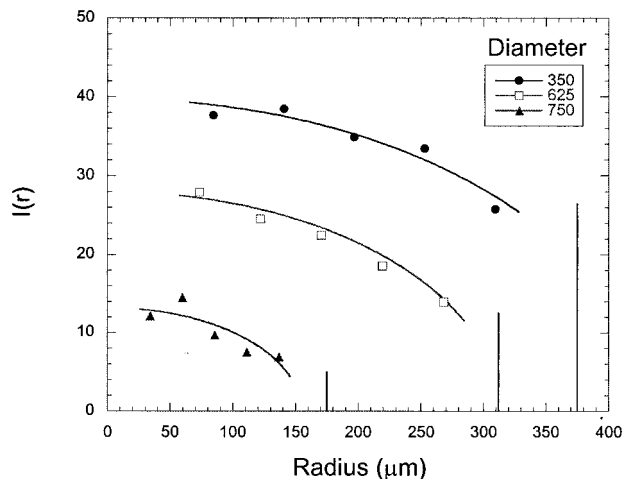


Fig. 15. Intensity dependence of the holographic features as a function of radius from the center for three tumors of different size. The small tumor shows the weakest holograms and the largest tumor shows the the strongest holograms. All show a general decrease of average intensity toward the rim of the tumor. These results agree statistically with histology performed on separate tumors.

brightness, we first compensate for the exponential extinction suffered by the coherent propagation of the light through the tumor tissue. We achieved this by multiplying the hologram brightness by an exponential function of the tissue path length with an effective extinction coefficient that balances the hologram brightness around the geometric center of the spheroid. After compensation, the hologram brightness is integrated within shells of increasing radius from the geometric center of the spheroid. From these we extract the average brightness of the holographic features as a function of tumor radius for a selection of tumor sizes. The results of this analysis for three tumors with diameters of 350, 625, and 750 μm are shown in Fig. 15. All tumors show stronger brightness toward the center of the tumor, with gradually decreasing intensity approaching the rim. Furthermore, the smallest tumor showed only weak holographic features, whereas the large tumor showed the brightest.

These results may be a measure of the increased necrotic density toward the center of the tumor spheroids that is observed in histology on similar tumors. The outer shell of healthy osteoblasts present a mostly homogeneous medium with weak speckle arising from cell membranes and cell organelles. Inside the tumor, microcalcifications and necrotic voids present a strongly heterogeneous medium with strong scatter that is seen as increased brightness of internal features relative to surface features. Small spheroids with diameters of 300–400 μm have the fewest and weakest necroses. The statistical analysis of the speckle features from the tumor spheroids therefore agrees with the overall morphology of the tumor spheroids, but it remains to identify features that are larger than the system optical resolution

that may represent an extended structure inside the tumors. This is the subject of future research.

5. Conclusion

We presented holographic images in reflection from coherence-gated depths within living tissue. All previous holographic recording of biological tissue has either been in transillumination or else without coherence gating in reflection. Holographic OCI therefore presents the first depth-resolved holograms of its kind to our knowledge. Our ability to record diffuse reflection holograms is a consequence of the high sensitivity of the PRQW devices. These devices exhibit the largest dynamic holographic sensitivity of any known material. The development of holographic OCI with these sensitive films provides a complementary imaging modality to OCT. Holographic imaging is direct, intrinsically *en face*; and fundamentally parallel in that it records multiple spatial modes simultaneously. Furthermore, the simultaneous acquisition of multiple spatial modes provides a means to record spatial phase coherences within tissue that is inaccessible to OCT.

Our chosen targets of multicellular tumor spheroids have the advantage of homogeneity and laboratory control over shape and size that are essential for parametric studies of a new imaging modality. However, the homogeneity of the spheroid tissue provides no clear large-scale morphology (tissue contrast) with which to perform comparative histology, at least for the current generation of experiments. Nonetheless, the strong statistical dependences of necrotic density observed in histology of these tumors matches closely the statistical dependences observed in the brightness of the recorded holographic features.

Future developments in holographic OCI include improvements in the holographic films to remove optical defects from fabrication and the implementation of Fourier-domain holography to allow us to directly observe spatially coherent phase within tissue. These improvements will extend the range and sensitivity of the technique, as well as demonstrate unique capabilities.

This research was supported by the National Center for Research Resources of the National Institutes of Health under grant R21 RR15040-02 and by the National Science Foundation under grant ECS-0200424.

References

1. D. Huang, E. A. Swanson, C. P. Lin, J. S. Schuman, W. G. Stinson, W. Chang, M. R. Hee, T. Flotte, K. Gregory, C. A. Puliafto, and J. G. Fujimoto, "Optical coherence tomography," *Science* **254**, 1178–1181 (1991).
2. J. G. Fujimoto, M. E. Brezinski, G. J. Tearney, S. A. Boppart, B. Bouma, M. R. Hee, J. F. Southern, and E. A. Swanson, "Optical biopsy and imaging using optical coherence tomography," *Nat. Med.* **1**, 970–972 (1995).
3. J. A. Izatt, M. D. Kulkarni, H.-W. Wang, K. Kobayashi, and M. V. Sivak, "Optical coherence tomography and microscopy in

- gastrointestinal tissues," *IEEE J. Sel. Top. Quantum Electron.* **2**, 1017–1028 (1996).
4. J. A. Izatt, M. D. Kulkarni, K. Kobayashi, M. V. Sivak, J. K. Barton, and A. J. Welch, "Optical coherence tomography for biodiagnosics," *Opt. Photon. News* **8**, 41–47 (1997).
 5. J. M. Schmitt and S. H. Xiang, "Cross-polarized backscatter in optical coherence tomography of biological tissue," *Opt. Lett.* **23**, 1060–1062 (1998).
 6. A. G. Podoleanu, J. A. Rogers, and D. A. Jackson, "OCT *en-face* images from the retina with adjustable depth resolution in real time," *IEEE J. Sel. Top. Quantum Electron.* **5**, 1176–1184 (1999).
 7. W. Drexler, U. Morgner, R. K. Ghanta, F. X. Kartner, J. S. Schuman, and J. G. Fujimoto, "Ultrahigh-resolution ophthalmic optical coherence tomography," *Nat. Med.* **7**, 502–507 (2001).
 8. M. R. Hee, D. Huang, E. A. Swanson, and J. G. Fujimoto, "Polarization-sensitive low-coherence reflectometer for birefringence characterization and ranging," *J. Opt. Soc. Am. B* **9**, 903–908 (1992).
 9. M. Laubscher, M. Ducros, B. Karamata, T. Lasser, and R. Salathe, "Video-rate three-dimensional optical coherence tomography," *Opt. Exp.* **10**, 429–435 (2002), <http://www.opticsexpress.org>.
 10. S. Bourquin, P. Seitz, and R. P. Salathe, "Optical coherence topography based on a two-dimensional smart detector array," *Opt. Lett.* **26**, 512–514 (2001).
 11. E. Beaurepaire, A. C. Boccara, M. Lebec, L. Blanchot, and H. Saint-Jalmes, "Full-field optical coherence microscopy," *Opt. Lett.* **23**, 244–246 (1998).
 12. E. N. Leith and J. Upatnieks, "Holograms: their properties and uses," in *Geometric Optics I*, H. R. Stoppach, ed., *Proc. SPIE* **4**, 3–6 (1965).
 13. H. Kogelnik, "Holographic image projection through inhomogeneous media," *Bell Syst. Tech. J.* **44**, 2451–2455 (1965).
 14. K. A. Stetson, "Holographic fog penetration," *J. Opt. Soc. Am.* **57**, 1060–1061 (1967).
 15. A. W. Lohmann and C. A. Schmalfuss, "Holography through fog: a new version," *Opt. Commun.* **26**, 318–321 (1978).
 16. M. A. Duguay and A. T. Mattick, "Ultra-high-speed photography of picosecond light pulses and echoes," *Appl. Opt.* **10**, 2162–2170 (1971).
 17. N. H. Abramson and K. G. Spears, "Single pulse light-in-flight recording by holography," *Appl. Opt.* **28**, 1834–1841 (1989).
 18. K. G. Spears, J. Serafin, N. H. Abramson, X. Zhu, and H. Bjelkhagen, "Chrono-coherent imaging for medicine," *IEEE Trans. Biomed. Eng.* **36**, 1210–1214 (1989).
 19. R. Jones, N. P. Barry, S. C. W. Hyde, P. M. W. French, K. M. Kwolek, D. D. Nolte, and M. R. Melloch, "Direct-to-video holographic readout in quantum wells for three-dimensional imaging through turbid media," *Opt. Lett.* **23**, 103–105 (1998).
 20. Z. Ansari, Y. Gu, J. Siegel, D. Parsons-Karavassilis, C. W. Dunsby, M. Itoh, M. Tziraki, R. Jones, P. M. W. French, D. D. Nolte, W. Headley, and M. R. Melloch, "High-frame-rate, 3-D photorefractive holography through turbid media with arbitrary sources and photorefractive structured illumination," *IEEE J. Sel. Top. Quantum Electron.* **7**, 878–886 (2001).
 21. S. C. W. Hyde, R. Jones, N. P. Barry, J. C. Dainty, P. M. W. French, K. M. Kwolek, D. D. Nolte, and M. R. Melloch, "Depth-resolved holography through turbid media using photorefraction," *IEEE J. Sel. Top. Quantum Electron.* **2**, 965–975 (1996).
 22. R. Jones, S. C. W. Hyde, M. J. Lynn, N. P. Barry, J. C. Dainty, P. M. W. French, K. M. Kwolek, D. D. Nolte, and M. R. Melloch, "Holographic storage and high background imaging using photorefractive multiple quantum wells," *Appl. Phys. Lett.* **69**, 1837–1839 (1996).
 23. D. D. Nolte, D. H. Olson, G. E. Doran, W. H. Knox, and A. M. Glass, "Resonant photodiffractive effect in semi-insulating multiple quantum wells," *J. Opt. Soc. Am. B* **7**, 2217–2225 (1990).
 24. D. D. Nolte, "Semi-insulating semiconductor heterostructures: optoelectronic properties and applications," *J. Appl. Phys.* **85**, 6259 (1999).
 25. D. D. Nolte, T. Cubel, L. J. Pyrak-Nolte, and M. R. Melloch, "Adaptive beam combining and interferometry with photorefractive quantum wells," *J. Opt. Soc. Am. B* **18**, 195–205 (2001).
 26. I. Lahiri, L. J. Pyrak-Nolte, D. D. Nolte, M. R. Melloch, R. A. Kruger, G. D. Bacher, and M. B. Klein, "Laser-based ultrasound detection using photorefractive quantum wells," *Appl. Phys. Lett.* **73**, 1041–1043 (1998).
 27. Y. Ding, R. M. Brubaker, D. D. Nolte, M. R. Melloch, and A. M. Weiner, "Femtosecond pulse shaping by dynamic holograms in photorefractive multiple quantum wells," *Opt. Lett.* **22**, 718–720 (1997).
 28. Y. Ding, D. D. Nolte, M. R. Melloch, and A. M. Weiner, "Time-domain image processing using dynamic holography," *IEEE J. Sel. Top. Quantum Electron.* **4**, 332–341 (1998).
 29. Y. Ding, A. M. Weiner, M. R. Melloch, and D. D. Nolte, "Adaptive all-order dispersion compensation of ultrafast laser pulses using dynamic spectral holography," *Appl. Phys. Lett.* **75**, 3255–3257 (1999).
 30. R. Jones, M. Tziraki, P. M. W. French, K. M. Kwolek, D. D. Nolte, and M. R. Melloch, "Direct-to-video holographic 3-D imaging using photorefractive multiple quantum well devices," *Opt. Exp.* **2**, 439–448 (1998), <http://www.opticsexpress.org>.
 31. R. Jones, N. P. Barry, S. C. W. Hyde, M. Tziraki, J. C. Dainty, P. M. W. French, D. D. Nolte, K. M. Kwolek, and M. R. Melloch, "Real-time 3-D holographic imaging using photorefractive media including multiple-quantum-well devices," *IEEE J. Sel. Top. Quantum Electron.* **4**, 360–369 (1998).
 32. Z. Ansari, Y. Gu, M. Tziraki, R. Jones, P. M. W. French, D. D. Nolte, and M. R. Melloch, "Elimination of beam walk-off in low-coherence off-axis photorefractive holography," *Opt. Lett.* **26**, 334–336 (2001).
 33. P. Yu, M. Mustata, W. Headley, D. D. Nolte, J. J. Turek, and P. M. W. French, "Optical coherence imaging of rat tumor spheroids," in *Coherence Domain Optical Methods in Biomedical Science and Clinical Applications VI*, V. V. Tuchin, J. A. Izatt, and J. G. Fujimoto, eds., *Proc. SPIE* **4619**, 210–218 (2002).
 34. P. Yu, M. Mustata, P. M. W. French, J. J. Turek, M. R. Melloch, and D. D. Nolte, "Holographic optical coherence imaging of tumor spheroids," *Appl. Phys. Lett.* **83**, 575–577 (2003).
 35. P. Yu, L. Peng, M. Mustata, J. J. Turek, M. R. Melloch, and D. D. Nolte, "Time-dependent speckle in holographic optical coherence imaging and the health of tumor tissue," *Opt. Lett.* **29**, 68–70 (2004).
 36. L. Vabre, A. Dubois, and A. C. Boccara, "Thermal-light full-field optical coherence tomography," *Opt. Lett.* **27**, 530–532 (2002).
 37. L. de Ridder, "Autologous confrontation of brain tumor-derived spheroids with human dermal spheroids," *Anticancer Res.* **17**, 4119–4120 (1997).
 38. K. Groebe and W. Mueller-Klieser, "On the relation between size of necrosis and diameter of tumor spheroids," *Int. J. Radiat. Oncol. Biol. Phys.* **34**, 395–401 (1996).
 39. R. Hamamoto, K. Yamada, M. Kamihira, and S. Iijima, "Differentiation and proliferation of primary rat hepatocytes cultured as spheroids," *J. Biochem. (Tokyo)* **124**, 972–979 (1998).
 40. G. Hamilton, "Multicellular spheroids as an *in vitro* tumor model," *Cancer Lett.* **131**, 29–34 (1998).
 41. P. Hargrave, P. W. Nicholson, D. T. Delpy, and M. Firbank, "Optical properties of multicellular tumour spheroids," *Phys. Med. Biol.* **41**, 1067–1072 (1996).
 42. L. A. Kunz-Schughart, M. Kreutz, and R. Knuechel, "Multicellular spheroids: a three-dimensional *in vitro* culture system to study tumour biology," *Int. J. Exp. Pathol.* **79**, 1–23 (1998).